

# LIGHT-ROBUST POLE-FROM-SILHOUETTE ALGORITHM AND VISUAL-HULL ESTIMATION FOR AUTONOMOUS OPTICAL NAVIGATION TO AN UNKNOWN SMALL BODY

Saptarshi Bandyopadhyay<sup>\*,§</sup>, Jacopo Villa<sup>†,§</sup>, Alan Osmundson<sup>‡,§</sup>,  
Benjamin Hockman<sup>\*,§</sup>, Benjamin Morrell<sup>\*</sup>, Daniel Lubey<sup>\*</sup>, Shyam Bhaskaran<sup>\*</sup>,  
David Bayard<sup>\*</sup>, Jay McMahon<sup>§</sup>, Issa A. Nesnas<sup>\*</sup>

We present a novel Pole-from-Silhouette (PfS) algorithm, which is robust to non-zero sun phase and illumination conditions like shadows. PfS is an important step in the optical navigation pipeline for an autonomous small spacecraft to approach an unknown small body. The algorithm estimates the rotation pole and 3D shape (visual hull) of a small body using only the illuminated pixels within the silhouette of the small body, the body’s rotation rate, the spacecraft attitude, and the spacecraft-target relative distance, which is estimated from orbit determination. We present detailed numerical simulations and multiple sensitivity analyses to demonstrate the effectiveness of our proposed PfS algorithm in different scenarios and target bodies.

## INTRODUCTION

A number of missions to small bodies have been launched (e.g. NASA’s OSIRIS-REx mission to near-Earth asteroid Bennu,<sup>1</sup> JAXA’s Hayabusa2 mission to near-Earth asteroid Ryugu,<sup>2</sup> NASA’s NEAR Shoemaker mission to the near-Earth asteroid Eros,<sup>3</sup> and ESA’s Rosetta mission to comet 67P/Churyumov–Gerasimenko<sup>4</sup>), that have performed rendezvous and proximity operations at small bodies, and currently returning samples from Bennu and Ryugu. Future missions to challenging targets like NASA’s Janus mission to two pairs of binary asteroids<sup>5</sup> and NASA’s DART mission to impact the secondary body of the Didymos system<sup>6</sup> are currently being planned. A common attribute in all these missions is that the spacecraft needs to be navigated through continuous ground-in-the-loop operations, to approach and rendezvous with the small body from deep space.

Since small bodies are thought to be time-capsules that encode the state of the Solar System at the time of their formation, we would like to explore the thousands of easily-reachable small bodies<sup>7</sup> to understand the evolution of the Solar System and hypothesize about the origin of life. At the same time, small bodies represent a target of interest for *in-situ* resource utilization and a key subject for planetary defense, given the potential hazard they pose for the Earth.<sup>8</sup> But the above intensive ground-in-the-loop operations approach does not scale well for a large number of missions to small bodies. Our prior work introduced a novel optical navigation pipeline (see Figure. 1) for an autonomous small spacecraft to approach an unknown small body, without requiring ground-in-the-loop for reaching and landing on the target, but which engages ground for goal setting and oversight when needed.<sup>9,10</sup>

When the spacecraft is far away from the small body and the small body’s image size is between 10s–100s of pixels, there is not enough resolution in the images to track relative-navigation features on the surface of the small body. But the clear boundary (silhouette) of the small body against the dark background of space contains valuable information about the size and shape of the small body. In turn, this can be used to

\*Jet Propulsion Laboratory, California Institute of Technology, 4800 Oak Grove Drive, Pasadena, CA 91109, USA

†University of Colorado Boulder, 3775 Discovery Drive, Boulder, CO 80303, USA

‡University of Southern California, Los Angeles, CA 90089, USA

§Contributed Equally

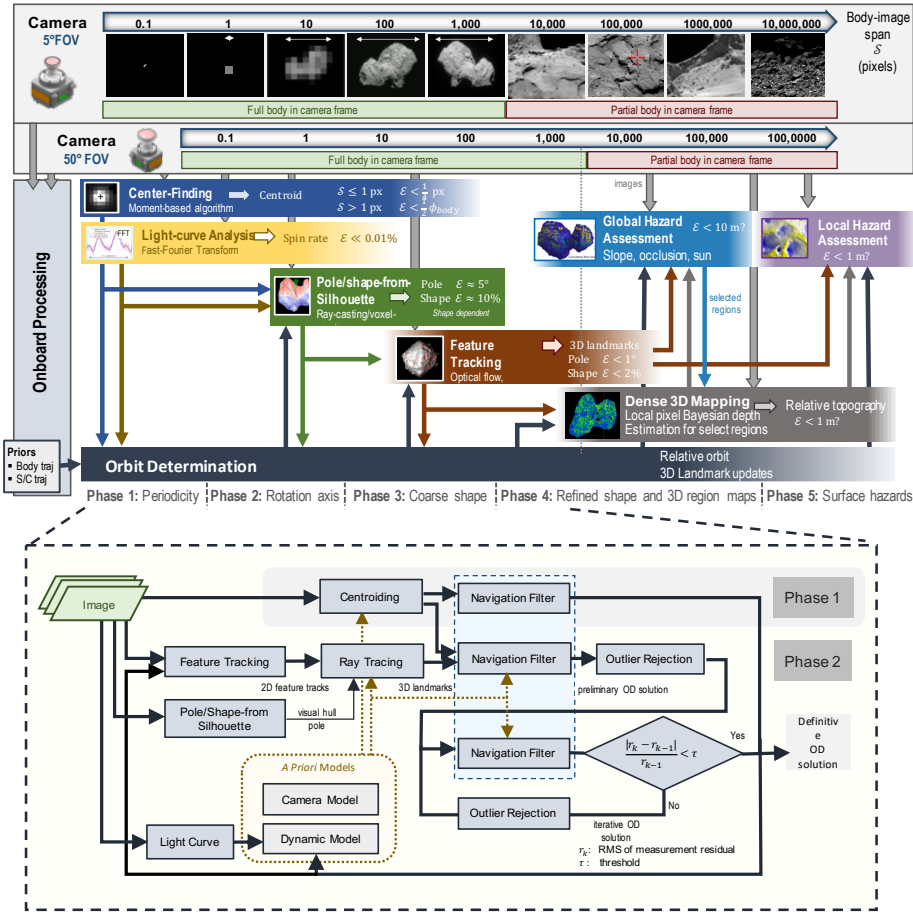


**Figure 1:** A multi-phase single-spacecraft and target body estimation framework (top) with details of the autonomous orbit determination process (bottom)<sup>9,10</sup>

estimate the body’s visual hull, the pole, and the centroid as seen from the camera. Our prior work introduced a novel Shape-from-Silhouette (SfS) algorithm, using voxel carving, that could estimate the functional 3D shape (visual hull) and the rotation pole of the small body.<sup>11</sup> In this paper, we present advances in Pole-from-Silhouette (PFS) and SfS algorithms, which are significantly faster than our prior algorithm<sup>11</sup> and more robust and effective in a variety of real-world situations.

The main inputs to the PFS algorithm are (i) a time-stamped sequence of images taken by the spacecraft during approach, (ii) the angular-velocity magnitude of the small body, (iii) the spacecraft attitude, and (iv) the distance of the spacecraft to the small body. All such parameters can be estimated onboard, as discussed in the following. The PSF algorithm outputs multiple hypotheses of the small body pole, that the later algorithms in the optical navigation pipeline need to check. The SfS algorithm generates a functional 3D shape (visual hull) for each of the pole hypotheses of the PSF algorithm. These algorithms are explained in detail in *Section Pole-from-Silhouette (Pfs) and Shape-from-Silhouette (Sfs) Algorithms*. These algorithms address a number of technical challenges in the optical navigation pipeline shown in Figure. 1, as discussed below:

1. PFS generates the first hypotheses of the pole of the small body, using very limited prior knowledge. These hypotheses are necessary for initializing the linear orbit determination (OD) filters. Absence of this information could cause the linear filters to diverge.
2. The visual hull generated by SfS is used by the OD algorithm to initialize the location of the features and landmarks. Absence of this information will force the OD algorithm to initialize features at the centroid (or some other arbitrary location), thereby affecting its performance.

3. The visual hull generated by SfS is also used to initialize the higher-fidelity shape estimate generated by the feature tracking and dense-3D-mapping algorithms.
4. The visual hull generated by SfS can enhance centroiding performance and help in estimating the center of mass of the small body.

Although the above steps might not be necessary for the traditional Stereophotoclinometry (SPC) approach to tracking small body mission using ground operations, PfS and SfS do have the capability to make these operations autonomous, more computationally efficient, and boot-strap some of the feature tracking processes.

### Literature Survey

Shape-from-Silhouette was first proposed in 1983 by Martin et al.<sup>12</sup> and has been improved over the past decades. Today, SfS is an established technique in computer vision, and has been successfully used within a broad spectrum of applications.<sup>13-15</sup> Whilst this algorithm is based on a powerful key principle, it also presents a fundamental limitation in terms of shape reconstruction. As firstly shown by Laurentini,<sup>16</sup> when using silhouette observations of the body to reconstruct its shape, it is not possible to recover local concavities on the body surface. Rather, the best obtainable shape is the convex surface surrounding the actual shape. This implies that, despite the number of observed silhouette and image resolution, the reconstructed shape will always be a conservative estimate of the actual shape, i.e. the estimated volume is always higher or equal to the true volume. This discrepancy increases the more concavities are present in the body, whereas the visual hull coincides with the true shape when the latter is convex.

SfS has also proven effective in applications involving small body imaging. The contrast between the dark background of space and the bright target body in the foreground makes these scenarios ideal to easily extract and use the body silhouette. SfS has been successfully employed during the Rosetta mission, both during the flyby with the asteroid Lutetia<sup>17</sup> and while approaching comet 67P.<sup>18</sup> The Rosetta team used orbital data not only to perform the standard SfS process, but also to account for the effect of the sun phase on the body appearance which, for non-zero phases, presents a dark side and hence shadowed pixels within the body silhouette. Identifying pixels belonging to the body's dark side is crucial to achieve proper silhouette extraction. We use the phase-robustness method proposed for the Lutetia flyby and generalize the results, testing the algorithm on a broad range of bodies, mission geometries and lighting conditions.

Previous work has also shown that SfS techniques are suitable to be run autonomously, using data that can be available onboard<sup>11</sup> and demonstrated their potential when used as a building block of an autonomous-navigation pipeline to approach a small body.<sup>9</sup> Autonomous shape modeling can be used for pole and landmark initialization, which in turn provides constraints for autonomous vision-based navigation. Starting from these works, we present a novel algorithm with superior computation performance and show how PfS (and its SfS subroutine) outputs can be used not only to inform navigation routines, but also to perform optical measurements computing the centroid via the estimated shape and pole.

### Main Contributions

The main contributions of this paper are in the following areas:

1. We present novel PfS and SfS algorithms in *Sections Pole Estimation using PfS Algorithm and Visual Hull Estimation using SfS Algorithm* that are robust to real-world scenarios like sun-angle variation, observation-latitude variation, etc. We generalize the shape estimation approach proposed by Lauer et al.<sup>17</sup> and show that it can successfully be applied throughout the whole domain of lighting conditions affecting the small body approach scenario. Higher sun phases yield more surface shadows, which interfere with the apparent silhouette of the body. By using knowledge from attitude and orbit determination, the algorithm predicts shadowed regions within the silhouette and excludes such pixels from the shape estimation routine. This process is called shadow casting, and provides a pole (and hence visual hull) estimate with little-to-no bias from surface illumination as shown in *Section Shadow Casting Algorithm for High Sun Phase Angles*.
2. We use a novel silhouette consistency evaluation routine, based on ray casting, which works on a 2D space, rather than on the voxel 3D space. This reduction in dimensionality drastically decreases

computation time for pole-likelihood evaluation. We envisage that this advanced SfS algorithm, that is significantly faster than the algorithms proposed in our previous autonomous work<sup>9,11</sup> and could be run onboard a small spacecraft, could help pave the way for autonomous small-spacecraft exploration of multiple small bodies.

3. In *Section Centroiding Algorithm using Pfs and Sfs outputs*, we present a novel method to accurately estimate the centroid of the small body using the outputs of the Pfs and Sfs algorithms and cross-correlations with the real images.
4. We discuss the sensitivity of the algorithms to different shapes of small bodies in *Section Sensitivity to Different Shapes* and show that symmetric small-body shapes give rise to multiple pole likelihoods.
5. We discuss the sensitivity of the algorithms to different image sizes of small bodies in *Section Sensitivity to Image Size* and show that for an asymmetric small-body, the Pfs algorithm can estimate the pole when the image size (span) is just 10 pixels.
6. We demonstrate in *Section Application to Real Trajectory from the Rosetta Mission* that these algorithms can be run autonomously (i.e. without human intervention) and are a suitable building block within an autonomous optical navigation pipeline.

In addition, we provide further explanations of concepts that are known in the computer-science literature, but are currently not well-understood in the guidance-navigation-control (GNC) literature:

7. SfS does not reconstruct the true shape of the small-body, and instead only generates an approximate shape model called the visual hull.<sup>16</sup> The difference between the true shape and the visual hull shape model of the small body, for different approach trajectories of the spacecraft, are explained in *Section Difference Between True Shape and Visual Hull*.
8. The spinning dancer illusion<sup>19</sup> creates an illusory pole during the Pfs process, which is explained with theoretical analysis in *Section Spinning Dancer Illusion*. It is possible to disambiguate between these two pole using a spacecraft trajectory maneuver to change the observation latitude.

## **POLE-FROM-SILHOUETTE (PFS) AND SHAPE-FROM-SILHOUETTE (SFS) ALGORITHMS**

The Pfs algorithm (see *Section Pole Estimation using Pfs Algorithm*) estimates the small body's pole by evaluating the pole likelihood for multiple hypotheses. The Sfs algorithm (see *Section Visual Hull Estimation using Sfs Algorithm*) estimates the visual hull of the small body, based on the maximum-likelihood pole previously estimated. The inputs to these algorithms are:

1. A stack of images of the target small body, captured by the spacecraft's camera.
2. An estimate of the rotation rate (angular velocity magnitude) of the small body. This is easily obtained by analyzing the frequency-component in the light-curve of the small body. We assume that the small body is performing pure rotation about its pole, i.e. the small body is not tumbling.
3. An estimate of the spacecraft attitude, usually provided by star trackers.
4. An estimate of the relative distance between the small body and the spacecraft, which can be obtained using the Orbit Determination (OD) algorithms running onboard the spacecraft.<sup>9,10,20</sup>
5. An estimate of the Sun phase angle on the small body, which can be obtained from the knowledge of the location of the small body, the spacecraft, and the Sun.

The outputs of these algorithms are:

1. The best estimates of the target body's rotation pole (i.e. there could be multiple good pole estimates).
2. The 3D visual hull of the small body for each of the pole estimates.

We first explain the difference between true shape and visual in the next section.

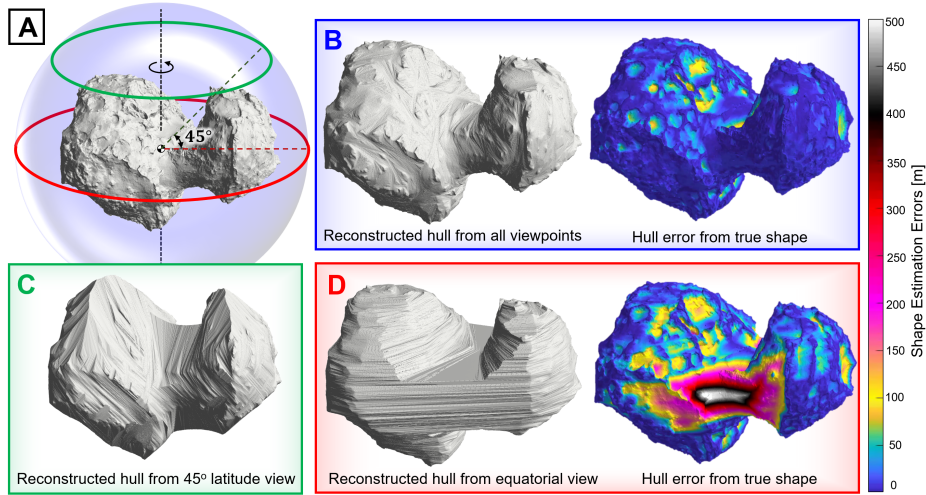


**Figure 2:** Visual hulls produced by the intersection of projected silhouettes from different viewing geometries. (A) The true shape of comet 67P with three observational latitudes/geometries are indicated. (B) The maximum observable visual hull from all viewing angles around the body, (C) the visual hull produced from images at a fixed latitude of  $45^\circ$ , (D) the visual hull produced from equatorial images only. Figs. (B) and (D) also show the shape error distribution (Hausdorff distance) of the visual hulls with respect to the true shape.

### Difference Between True Shape and Visual Hull

When using silhouettes to estimate a volumetric representation of the target, the output shape does not necessarily coincide with the true shape. As firstly discussed by Laurentini,<sup>16</sup> SfS techniques can only recover the target shape up to its visual hull. The visual hull is the convex shape estimated by a given set of silhouette observations, such the projection of the hull in the camera field of view yields the silhouette observed for a given viewpoint. Hence, the concavities on the true shape (e.g. craters) are not captured from the visual hull, which is a convex surface. Thus, the volume of the visual hull will always be higher than the volume of its original shape, unless the latter is a fully-convex body. In this last case, the visual hull coincides with the original shape.

In this context, the perfect visual hull, i.e. the one where the error with respect to the true shape is minimum, is obtained when the shape observability is maximized. This occurs when the silhouette viewpoints are sufficient in number and sufficiently spread around the body shape. For the approach phase of a mission toward a small body, the viewpoints depend upon the approach geometry. For example, if a spacecraft is approaching a principal-axis-rotator body along its equatorial plane (i.e. the approach latitude is zero), the camera viewpoints are such that the observed silhouettes do not capture concavities in the equatorial region. Similarly, a polar approach latitude would make concavities close to the pole unobservable. When surface traits are not captured by the silhouettes, shape artifacts are generated by the algorithm, increasing shape modeling error. Figure 2 shows examples of visual hulls of comet 67P constructed from different observational latitudes. Hulls reconstructed from a limited range of latitudes tend to have larger shape anomalies, though even the maximum observable visual hull cannot resolve some surface concavities (e.g. craters).

Despite these limitations of the visual hull, SfS proves to be effective to both estimate a rough global shape model and to estimate the pole from a real trajectory, as discussed in *Section Application to Real Trajectory from the Rosetta Mission*. Note that advanced algorithms like the shadow carving technique,<sup>17</sup> used to further improve the visual hull estimate, are not used in this paper.

### Pole Estimation using PfS Algorithm

The key concept of PfS algorithm is to hypothesize multiple poles and observe their performance. If a bad hypothesis of the pole was used, then the comparison would be bad as shown in Figure 3a. On the other hand, if we serendipitously use a good hypothesis of the pole, then the comparison would be very good as shown in Figure 3b. We search over the entire space of poles (i.e. Right Ascension (RA)  $\in [-180^\circ, 180^\circ]$  and Declination (Dec)  $\in [-90^\circ, 90^\circ]$ ) and generate a likelihood of the pole as shown in Figure 6a. The best pole hypothesis is eventually used to perform visual hull estimation.

---

**Algorithm 1:** Ray-Cast Pole Evaluation Pseudocode

---

**input** Pole Hypothesis  $H(\alpha, \delta)$ ;  
 $N$  = Number of images in dataset;  
 $I_i$  = True image  $i$ ,  $\forall i \in \{1, \dots, N\}$ ;  
 $I_T$  = True image being checked for consistency, for some  $T \in \{1, \dots, N\}$ ;  
 $C_T$  = Camera frame corresponding to  $I_T$ ;  
Initialize  $I_P \leftarrow I_T$  = Map of consistent pixels;

**for** pixels  $(v, u)$  where  $(I_T(u, v) > 0)$  **do**  
  Create Ray  $\overrightarrow{p_{1C_T}p_{2C_T}}$  (cyan arrows in Figure 4a);  
  Convert pixels  $(v, u)$  in image  $I_T$  to  $(y_{C_T}, x_{C_T})$  in Camera frame  $C_T$ ;  
   $w$  = Estimated small body size in meters;  
   $d$  = Estimated distance from camera to small body in meters;  
   $p_{1C_T} \leftarrow (x_{C_T}, y_{C_T}, d - w)$ ;  
   $p_{2C_T} \leftarrow (x_{C_T}, y_{C_T}, d + w)$ ;  
  Rotate Ray  $\overrightarrow{p_{1C_T}p_{2C_T}}$  to Body frame  $\overrightarrow{p_{1B}p_{2B}}$  ;  
   $T_{C_T}^B$  = Rotation and translation from Camera frame  $C_T$ , corresponding to image  $I_T$ , to Body frame  $B$  using pole hypothesis  $H(\alpha, \delta)$ ;  
   $p_{1B} \leftarrow T_{C_T}^B p_{1C_T}$ ;  
   $p_{2B} \leftarrow T_{C_T}^B p_{2C_T}$ ;

**for** All Images  $i = 1 : N$  **do**  
    Rotate Ray  $\overrightarrow{p_{1B}p_{2B}}$  to Camera  $C_i$  frame  $\overrightarrow{p_{1C_i}p_{2C_i}}$  ;  
     $T_B^{C_i}$  = Rotation and translation from Body frame  $B$  to Camera frame  $C_i$ , corresponding to image  $I_i$ , using pole hypothesis  $H(\alpha, \delta)$ ;  
     $p_{1C_i} \leftarrow T_B^{C_i} p_{1B}$ ;  
     $p_{2C_i} \leftarrow T_B^{C_i} p_{2B}$ ;  
    Project Ray  $\overrightarrow{p_{1C_i}p_{2C_i}}$  into image plane of image  $I_i$ ;  
     $t$  = Size of one pixel of  $I_T$  in meters (thickness of the ray);  
    pixel array  $(\mathbf{m}, \mathbf{n})$  = 2D projection of Ray  $\overrightarrow{p_{1C_i}p_{2C_i}}$  with thickness  $t$  into the image plane of image  $I_i$ ;  
    Check if at least one pixel in pixel array  $(\mathbf{m}, \mathbf{n})$  is lit in image  $I_i$ ;  
    **if** no pixel in pixel array  $(\mathbf{m}, \mathbf{n})$  is lit in image  $I_i$  **then**  
      | Set  $I_P(v, u) \leftarrow 0$ ;  
    **end**  
  **end**

**end**  
**return**  $I_P$  (Consistent pixels in Figure 4b)

---

Previous work evaluating pole likelihood required 3D visual hull estimation as a first step.<sup>9,11</sup> Here, we present a novel algorithm to assess the most-likely pole hypotheses using only the 2D information in the observed silhouettes. This novelty substantially reduces computation time and simplifies the algorithm.

The pole estimation process is described in **Algorithm 1**. The key idea is that multiple pole hypotheses ( $H(\alpha, \delta)$ ), expressed in terms of pole's Right Ascension ( $\alpha$  or RA) and Declination ( $\delta$  or Dec), are evaluated. For each pole hypothesis, predictions are made on the upcoming silhouettes in the considered image set. The prediction is made as follows: each pixel in the initial silhouette is considered as an oblong parallelepiped seen from the front, where the observed pixel represents the basis surface. We call this object a *ray* and the following process *ray casting*. For a successive (new) silhouette, the camera-body relative pose changes, hence the ray is also rotated according to the hypothesized pole and known rotation rate. The rotation will

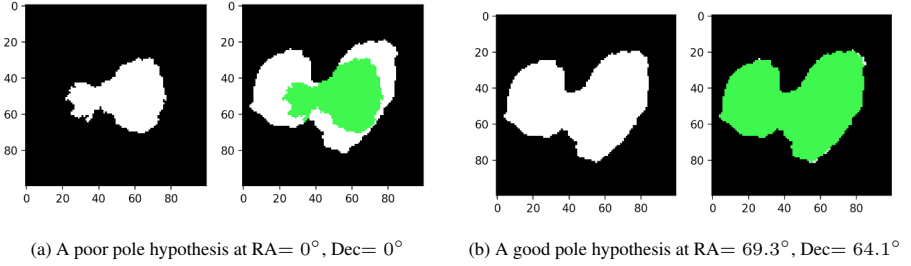
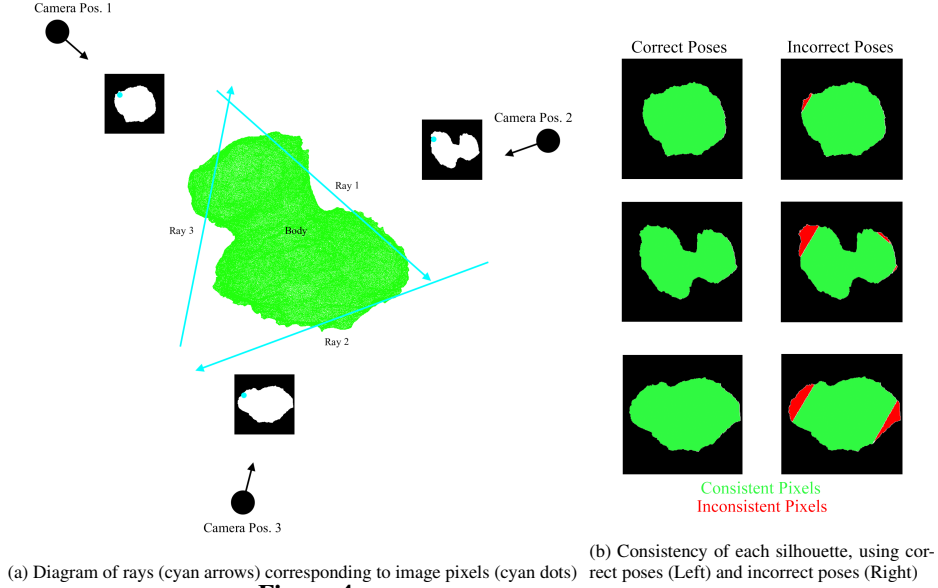


**Figure 3:** Comparison of output of **Algorithm 1** for two pole hypotheses. The left image is the observed silhouette with all inconsistent pixels removed, and the right image shows it overlaid onto the original observed silhouette. Here the small body is 67P/CG.

make the ray appear with a new perspective where the parallelepiped will span more than 1 pixel in the camera field of view. See **Figure 4** and **5** for a pictorial explanation.



(a) Diagram of rays (cyan arrows) corresponding to image pixels (cyan dots) rect poses (Left) and incorrect poses (Right)

**Figure 4:** Explanation of the ray casting process

At this point, the overlap between the new silhouette and the rotated ray, projected onto the camera plane, is computed: since the ray is generated starting from an originally-lit pixel, if the pole hypothesis is correct, the ray needs to overlap with at least one lit pixel even in the new silhouette. Based on this principle, a consistency-score image ( $I_P$  in **Algorithm 1**) is generated: pixels fulfilling the above condition for all considered images are mapped with value 1; the other pixels are mapped as 0. This image is then compared to the observed (true) image and the overlap error ( $\epsilon$ ) between the two is computed as shown in Equation 1:

$$\epsilon = \frac{\sum ((I_{T_i} \cup I_{P_i}) - (I_{T_i} \cap I_{P_i}))}{\sum I_{T_i}} \quad (1)$$

The key principle here is that a better pole hypothesis yields to a higher overlap in the ray casting process. For example, see example in **Figure 6a**. Note that it is difficult to see the peaks in the overlap metric ( $\epsilon$ ). Hence, we define the relative pole likelihood in Equation 2:

$$\mathcal{L} = \epsilon^{-1} \quad (2)$$

The same example is shown in **Figure 6b**, where the four peaks are clearly visible.

Note that that multiple good pole estimates might co-exist, and they are all carried forward as multiple hypotheses by the optical navigation pipeline which will eventually disambiguate the correct solution. For example, as shown in **Figure 6** and **7**, we see four peaks for an approximately symmetric body.

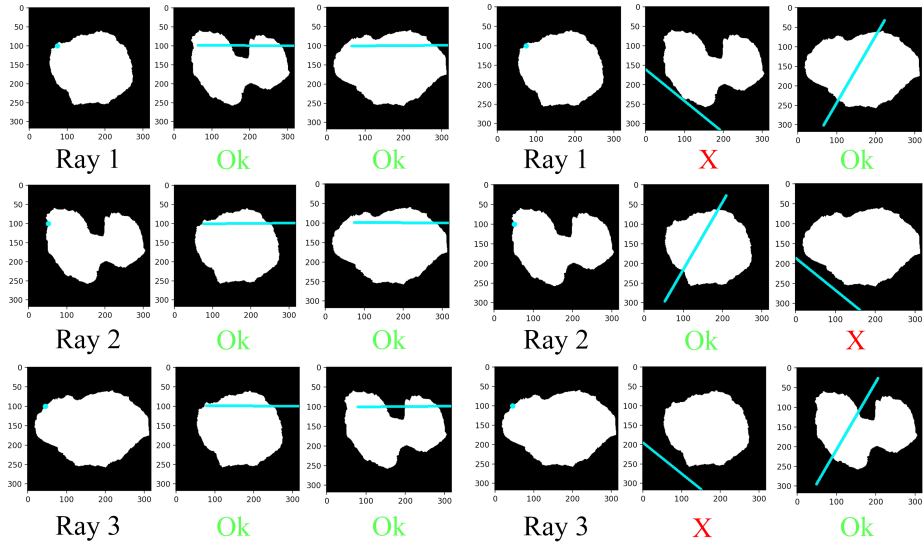
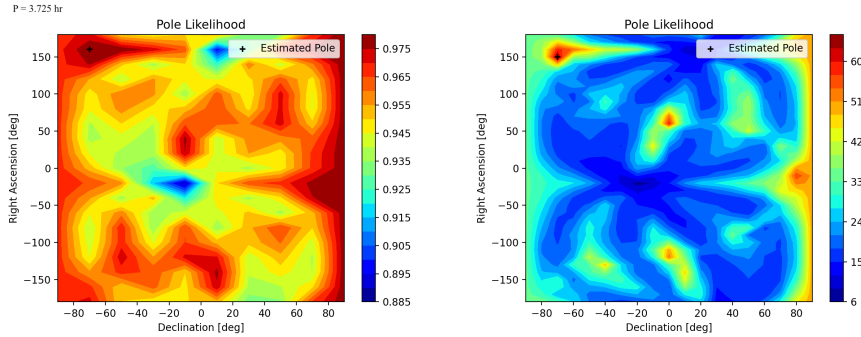


**Figure 5:** Projection of rays onto each other image, using correct poses (Left) and incorrect poses (Right). Rays which do not intersect the body for at least one image are deemed inconsistent.



(a) Overlap metric ( $\epsilon$ ) from Equation 1      (b) Pole likelihood ( $\mathcal{L}$ ) from Equation 2  
**Figure 6:** Advantages of relative pole likelihood ( $\mathcal{L}$ ) over the overlap metric ( $\epsilon$ )

### Visual Hull Estimation using SfS Algorithm

Once the maximum-likelihood pole is determined, it is used to estimate the target body’s visual hull. This is the standard SfS process presented in *Section Literature Survey*. For this step, we use the method presented by Villa et al.,<sup>9</sup> whose core algorithm is initially proposed by Forbes.<sup>21</sup> The key principle is as follows: using silhouettes of the body imaged from different points of view, and knowing the relative pose between camera and body (from PfS and the inputs previously listed), an implicit surface function is defined to estimate the visual hull. This is a boolean function which takes a query point in the body-centered, body-fixed frame as input, and returns *True* if the query point is inside the surface of the visual hull, or *False* if the point is outside. When a point is queried, it is projected onto every image, using the available poses. If, for any image, this projection falls on an empty pixel, the function returns *False*. If this does not happen for any image, i.e. the projection always falls on a lit pixel, the function returns *True*. This algorithm is listed in pseudocode in Algorithm 2. A

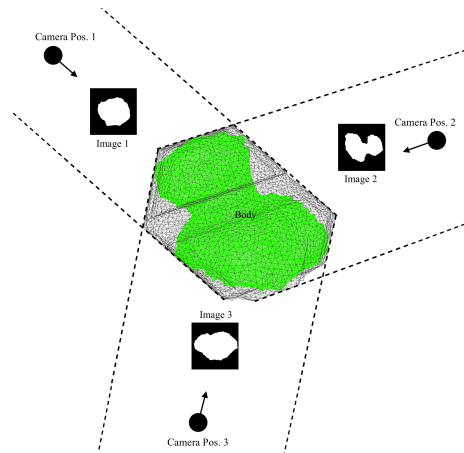


**Figure 8:** Functional representation of the small body’s shape is generated by Algorithm 2.

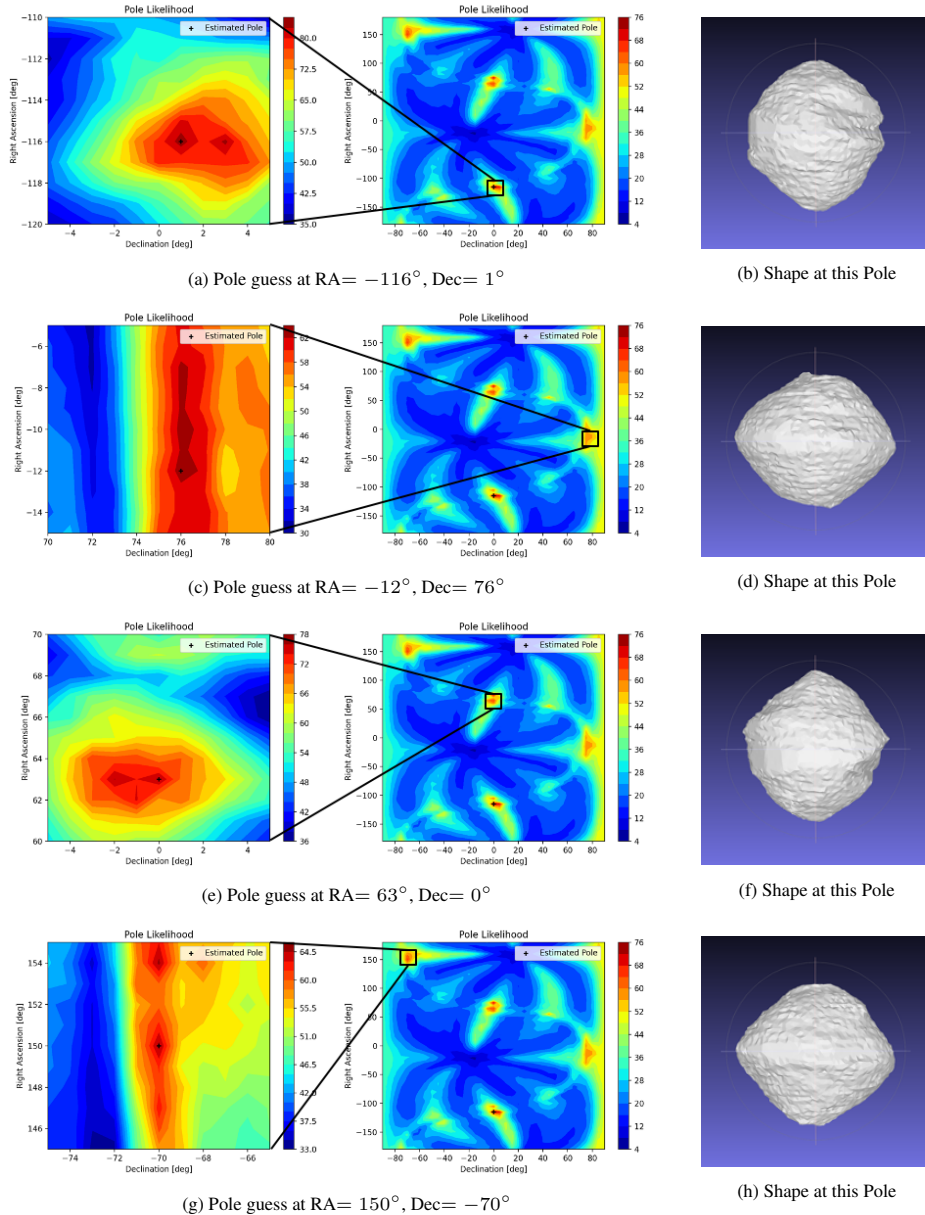


**Figure 7:** Shapes generated for an approximately symmetric small body by **Algorithm 2**, for the four peaks in pole likelihood plot

schematic representation of this functional representation is shown in Figure 8, where the camera position is represented in the small-body-fixed frame whilst it samples body silhouettes from multiple points of view.

Once this function is defined, it can be used as input for a polygonizer, which converts the boolean function into a polygon mesh, which is a format that can be more easily visualized and analyzed. We use a Marching Cube algorithm to convert the surface function into a triangle mesh. As shown in Figure 7, the 3D shape generated by each of these peaks looks reasonable and have to be evaluated/refined by the downstream pipeline.

To be noted that, while in previous work this voxel-carving process was run for all pole hypotheses,<sup>9,11</sup> this method has to be performed only a few times using the most-likely pole determined by PFS. This drastically decreases computation time and hence is more compelling for onboard autonomy.

### Shadow Casting Algorithm for High Sun Phase Angles

---

**Algorithm 2:** Visual Hull Implicit Surface Function

---

**input**  $p_B$  = Point to be evaluated in Body Frame  $B$  (body-centered body-fixed coordinates);  
 $N$  = Number of images in dataset;  
 $I_i$  = True image  $i$ ,  $\forall i \in \{1, \dots, N\}$ ;  
 $C_i$  = Camera frame corresponding to image  $I_i$ ;  
 $H(\alpha, \delta)$  = Pole Hypothesis;

**for** All images  $i = 1 : N$  **do**  
    Rotate Point  $p_B$  to Camera  $C_i$  frame  $p_{C_i}$  ;  
     $T_B^{C_i}$  = Rotation and translation from Body frame  $B$  to Camera frame  $C_i$ , corresponding to image  $I_i$ , using pole hypothesis  $H(\alpha, \delta)$ ;  
     $p_{C_i} \leftarrow T_B^{C_i} p_B$ ;  
    Project Point  $p_{C_i}$  into image plane of image  $I_i$ ;  
    pixel  $(v, u)$  = 2D projection of Point  $p_{C_i}$  into the image plane corresponding to image  $I_i$ ;  
    Check if pixel  $(v, u)$  is lit in image  $I_i$ ;  
    **if**  $I_i(v, u) = 0$  **then**  
        | **return** False  
    **end**  
**end**  
**return** True

---

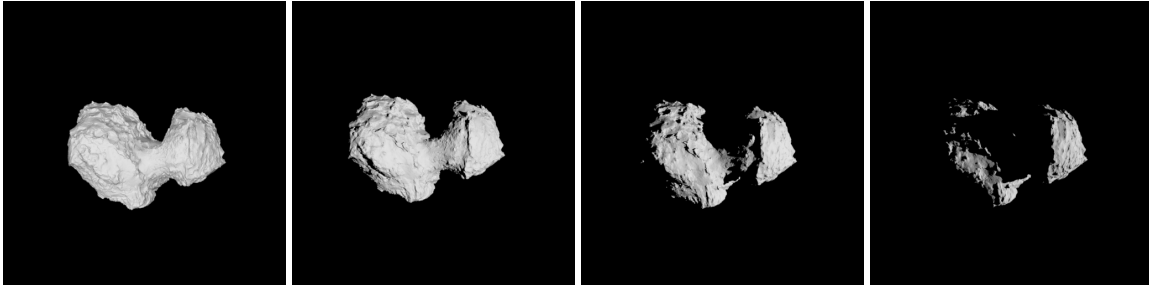


**Figure 9:** Simulated images of 67P/CG for  $0^\circ$ ,  $30^\circ$ ,  $60^\circ$ , and  $90^\circ$  Sun phase angles

Next we study the effect of different Sun phase angles and observing latitudes. Figure 9 shows multiple views of 67P/CG in different Sun phase angles. Note the shadows on the small body for high Sun phase angles. Figure 12 shows the error in pole estimate for increasing Sun phase angles, for four different observation latitudes ( $0^\circ$ ,  $30^\circ$ ,  $45^\circ$ , and  $60^\circ$ ). The concept of observational latitudes was introduced in Figure 2. The standard ray-casting PfS algorithm (from *Section Pole Estimation using PfS Algorithm*) seems to be robust up to  $20^\circ$  sun phase angle. But as the sun phase angle increases further, the performance of ray-casting PfS algorithm degrades.

In order to mitigate the effects of self-shading/shadows and high Sun phase angles, we create a new set of binary images using shadow casting. Using the known pose data of the camera and the sun in the inertial frame, we can determine the direction of the 2D sunlight vector on any given image  $i$ . A new, blank image is created with the same size as image  $i$ , then all pixels which are "behind" the illuminated limb, with respect to the sunlight vector, are set to 1. This illuminates all regions which could possibly be shadowed. Some examples are shown in Figure 11. Next, when PfS algorithm from *Section Pole Estimation using PfS Algorithm* is executed, where each unmodified image is compared against each shadow-cast image, i.e. in Algorithm 1,  $I_T$  is unmodified and  $I_i$  is shadow-cast. Figure 10 shows the overlap metric ( $\epsilon$

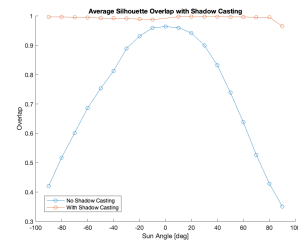


**Figure 10:** Silhouette overlap metric ( $\epsilon$  in Equation 2) as a function of the Sun phase angle. When shadow-casting is enabled, the bias introduced by shadows on the overlap metric is drastically reduced.

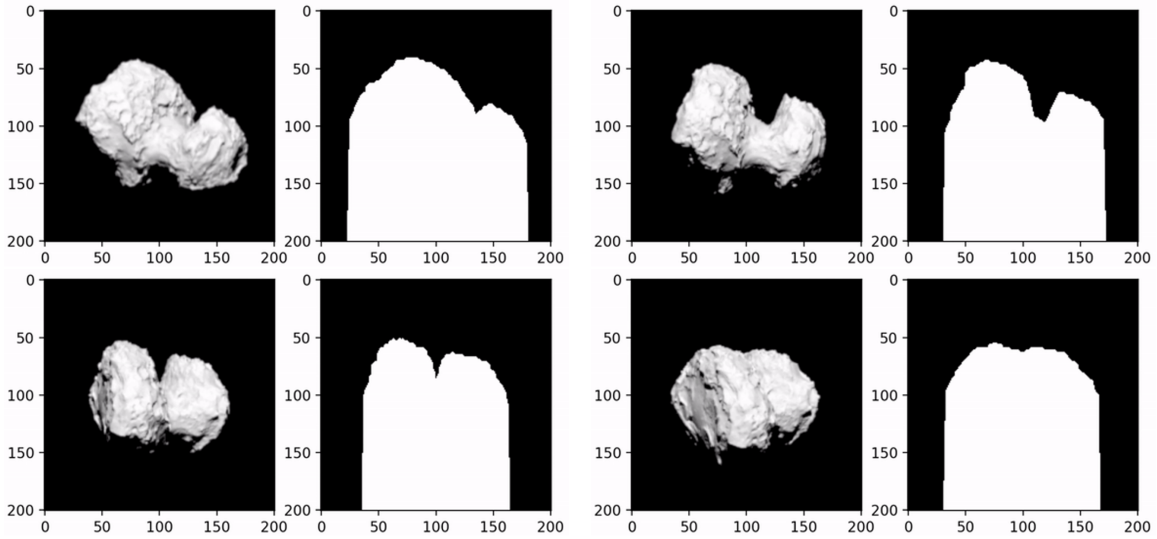


**Figure 11:** Examples of shadow casting. In all these examples, the true image is shown in the left, and the silhouette with shadow-casting enhancement is shown in the right. The position of the Sun is directly above the spacecraft, where the Sun phase angle is  $45^\circ$ .

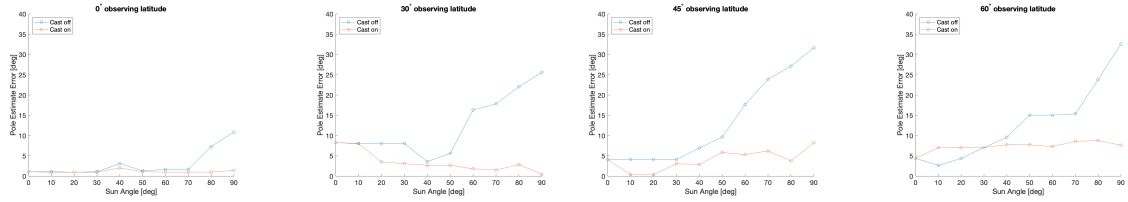


**Figure 12:** Pole estimate error vs. Sun phase angle, for comet CG, with and without shadow-casting, for  $0^\circ$ ,  $30^\circ$ ,  $45^\circ$ , and  $60^\circ$  observing latitude

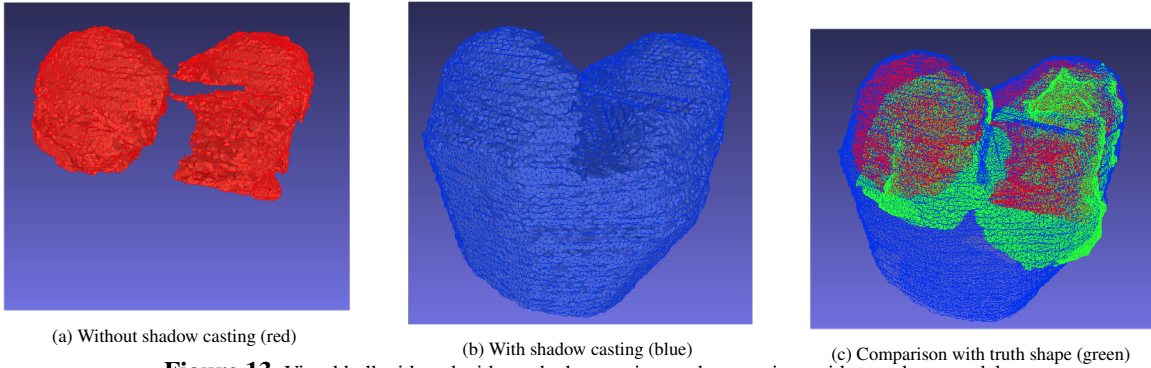


**Figure 13:** Visual hull with and without shadow casting, and comparison with true shape model

from Equation 1) under different Sun phase angles. This shadow-casting PfS algorithm greatly improves the pole estimation accuracy for high Sun phase angle trajectories and different observation latitudes, as shown in Figure 12.

Shadow casting also helps in generating better visual hull shapes, as shown in Figure 13. The shape generated without shadow casting is incomplete (i.e. not water-tight), as shown in Figure 13a. The shape generated with shadow casting is highly-conservative, but complete (i.e. water-tight), as shown in Figure 13b. Note that the shape generated with shadow casting is a conservative estimate of the true shape, as shown in Figure 13c.

### Centroiding Algorithm using PfS and SfS outputs

One potential application of SfS and PfS techniques for autonomous optical navigation is estimating the centroid of the unknown small body. These algorithms provide estimates of the body’s shape and pole which, combined with those of camera attitude and relative trajectory, can be used to predict the appearance of the target body in the camera field of view. Then, the predicted image of the body can be 2D cross-correlated with the observed image to estimate the centroid. The process of using cross-correlation for centerfinding is an established technique for extended-target optical navigation.<sup>22</sup> In standard practice, the predicted (synthetic) image is usually generated using high-fidelity reflectance models of the target body and ray tracing to maximize photorealism.<sup>23</sup> Here, we propose a less computationally expensive approach based on silhouette cross-correlation to compute the centroid, as described in **Algorithm 3**. This technique is less precise than the conventional method, but more amenable for onboard autonomy. Additionally, knowing the visual hull’s center of volume, it is possible to estimate the target body’s center of volume as well (see **Algorithm 3**).

---

#### Algorithm 3: Silhouette-Based Centroiding

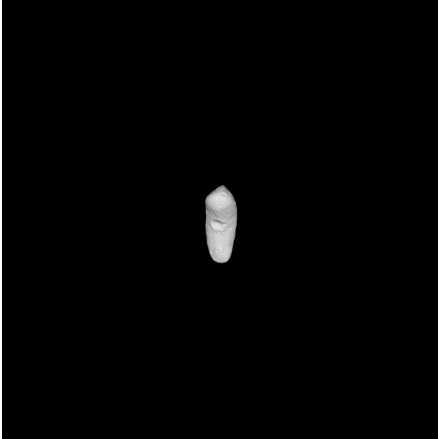
---

```

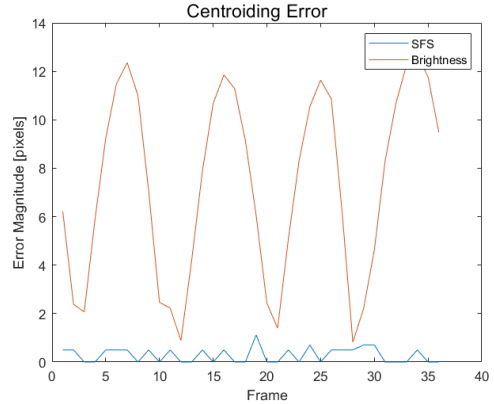
input Visual hull, Pole, Body’s Rotation Rate, Relative Trajectory, Camera Attitude;
for All Images  $i = 1 : N$  do
     $\mathcal{I}_P \leftarrow$  Predicted silhouette image, using inputs;
     $\mathcal{I}_O \leftarrow$  Observed silhouette image;
     $B \leftarrow$  Bounding box of predicted silhouette image;
     $\mathcal{I}_T \leftarrow$  portion of  $\mathcal{I}_P$  within  $B$ ;
     $\vec{c}_B \leftarrow$  2D center of the bounding box;
     $\vec{C}_{V0} \leftarrow$  3D center of volume of the visual hull;
     $\vec{c}_{V0} \leftarrow$  Project  $\vec{C}_{V0}$  onto the camera plane;
     $\beta \leftarrow \vec{c}_{V0} - \vec{c}_B$ ;
     $S \leftarrow \mathcal{I}_O * \mathcal{I}_T$  (convolution score of template with observed silhouette);
     $\vec{C}^* \leftarrow \max(S)$ (centroid coordinates in  $S$ );
     $\vec{C} \leftarrow \text{map } \vec{C}^* \text{ into } \mathcal{I}_O$ (Centroid coordinates in observed image);
     $\vec{C}_V \leftarrow \vec{C} + \beta$  (estimated center of volume);
end
return  $\vec{C}, \vec{C}_V$ 

```

---



(a) Sample synthetic image of the asteroid Eros.



(b) Evolution of the error norm for two algorithms: the brightness moment centroiding and the visual hull-based centroiding. The error is computed with respect to the body’s center of volume.

**Figure 14:** Centroiding simulation using SfS and PfS outputs, i.e. pole and visual hull.

We tested the above centroiding algorithm on a set of 40 synthetic images capturing the asteroid Eros (Figure 14a), from which we also estimated a visual hull and the pole using SfS and PfS. Here, we assume

that there is no initial error in the relative pose, hence we are only assessing the impact of shape modeling errors on centroiding. We compare centroiding performance to a brightness moment algorithm.<sup>22</sup> Results are shown in Figure 14b: despite its simplicity, the error of the visual hull-based method never exceeds one pixel and outperforms the brightness centroid. Moreover, by estimating the offset between center of figure and center of volume ( $\beta$ ), we are able to eliminate the periodic component in centroiding error, which is due to the body’s asymmetry. This and similar techniques could be suited for autonomous navigation when the target body’s resolution is relatively low. Future work will assess the impact of errors in input parameters on centroiding performance.

## SENSITIVITY ANALYSIS

In this section, we understand the sensitivity of the PfS and SfS algorithms to different shapes and image sizes of the small body (see Section *Sensitivity to Different Shapes* and Section *Sensitivity to Image Size*), and discuss a special ambiguity that arises due to a spacecraft’s straight approach trajectory (see Section *Spinning Dancer Illusion*).

### Sensitivity to Different Shapes

Since PfS algorithm only uses the silhouette of the small body, its performance is strongly affected by the symmetry of the small body’s shape. In this section, we explore this effect in detail.

For the simulations in this section, we use the triaxial ellipsoid shape model shown in Figure 15. The rotation pole is through the major axis of inertia (i.e. the principal axis with the highest moment of inertia, shown in blue in Figure 15). The stationary spacecraft observes from a latitude of  $45^\circ$ , and is sufficiently far away for the entire small body to be visible in the spacecraft’s camera-frame. The small-body is completely illuminated (i.e. the sun is along the small-body to spacecraft line and directly behind the spacecraft).

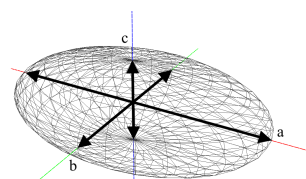


**Figure 15:** Triaxial ellipsoid shape model, where  $a$ ,  $b$ , and  $c$  represent the sizes of the three axes

*Perfectly-symmetric small-body shape (Sphere)* When the small body’s shape is perfectly symmetric (i.e. sphere with  $a = b = c$  in Figure 15), then the silhouette looks the same irrespective of the viewing angle. The resultant body shape and viewing geometry (in cyan) is shown in Figure 16(left).

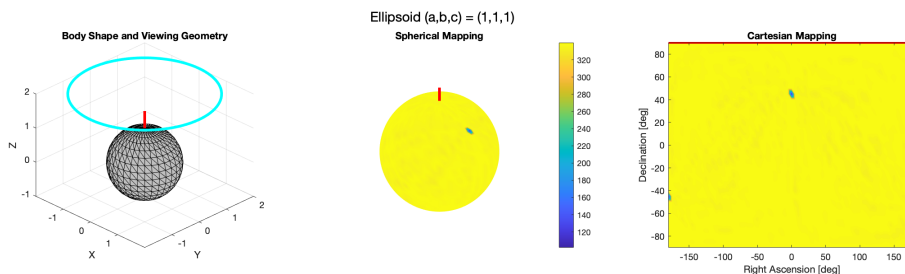


**Figure 16:** Shape model and pole likelihood for a spherical small-body shape ( $a = b = c$ )

Hence, PfS is unable to determine the pole orientation, as shown in Figure 16(middle and right), where the noisy distribution with no clear peaks at any pole orientations. Figure 16 shows two different methods of showing the same data: (right) shows the standard RA-Dec plot introduced in Section *Pole-from-Silhouette (PfS) and Shape-from-Silhouette (SfS) Algorithms* and (middle) shows the conformal mapping of this information onto a sphere. As will become obvious in the later sections, this process of visualizing the RA-Dec plot on a sphere helps us clearly see the bands of peaks.

*Two-axis-symmetric small-body shape* When two axes are symmetric (i.e.  $a = b \neq c$  in Figure 15), then four bands of peaks are visible on the RA-Dec plot as shown in Figures 19, 18, and 17. Two of these peaks are caused by the symmetry in the shape, and the other two peaks are caused by the ambiguity discussed in Section *Spinning Dancer Illusion*.

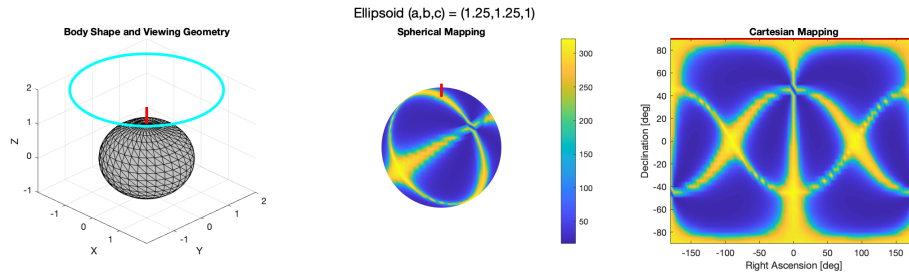


**Figure 17:** Shape model and pole likelihood for two-axis-symmetric shape ( $a = b = 1.25$  and  $c = 1$ )

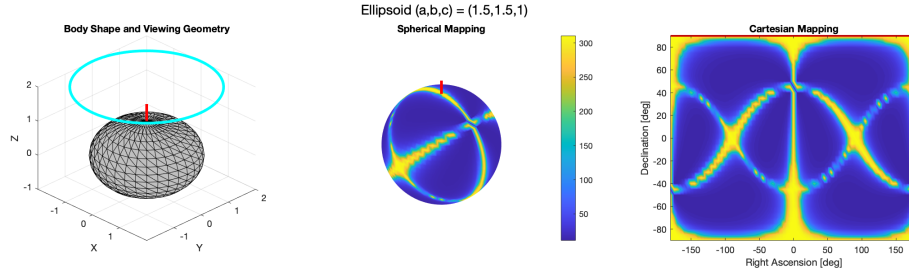


**Figure 18:** Shape model and pole likelihood for two-axis-symmetric shape ( $a = b = 1.5$  and  $c = 1$ )

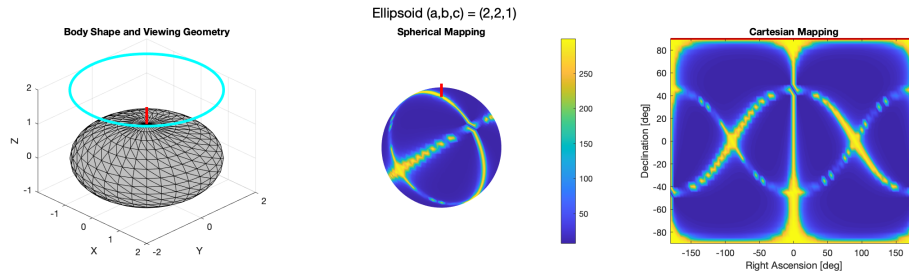


**Figure 19:** Shape model and pole likelihood for two-axis-symmetric shape ( $a = b = 2$  and  $c = 1$ )

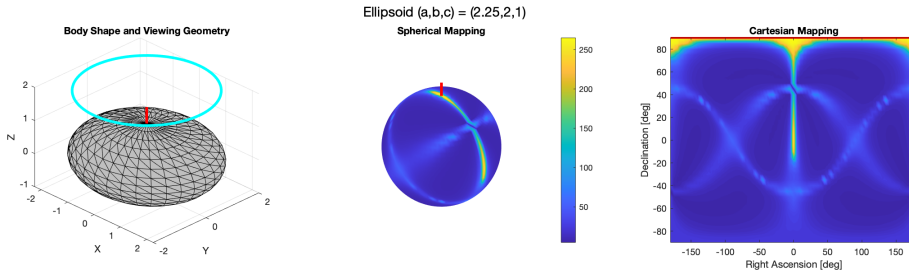


**Figure 20:** Shape model and pole likelihood for asymmetric shape ( $a = 2.25$ ,  $b = 2$ ,  $c = 1$ )

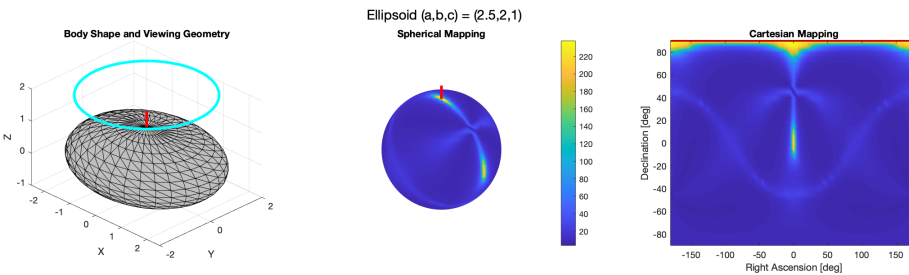


**Figure 21:** Shape model and pole likelihood for asymmetric shape ( $a = 2.5$ ,  $b = 2$ ,  $c = 1$ )

*Asymmetric small-body shape* When small body shape is asymmetric (i.e.  $a \neq b \neq c$  in Figure 15), then two bands of peaks are visible on the RA-Dec plot as shown in Figures 22, 21, and 20. These two peaks

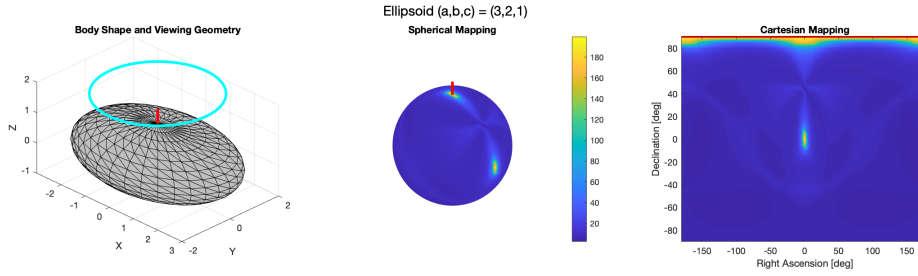


**Figure 22:** Shape model and pole likelihood for asymmetric shape ( $a = 3, b = 2, c = 1$ )

are caused by the ambiguity discussed in *Section Spinning Dancer Illusion*. Note that as  $a \rightarrow b$ , we see the formation of the two orthogonal bands as seen in the previous section.

*Double Cone Shape with Multiple Symmetries* Another small body shape with multiple axes of symmetry is the double cone example shown in Figure 23. This figure shows multiple bands of peaks, representing the different symmetries in the shape and the ambiguities.

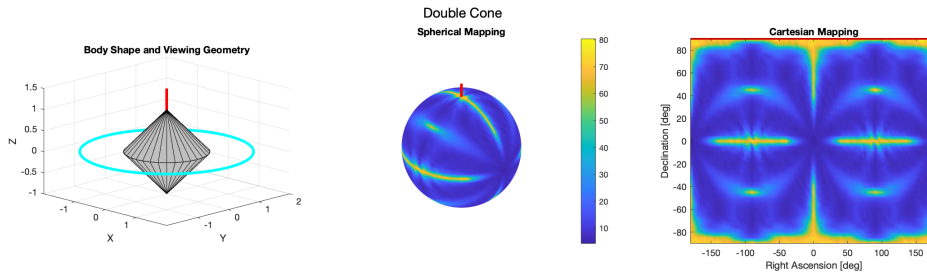


**Figure 23:** Double cone shape model and pole likelihood with multiple symmetries

Hence we conclude that if the pole likelihood plot shows multiple bands with peaks, then there must be some symmetry in the small body's shape.

### Spinning Dancer Illusion

The spinning dancer illusion (or silhouette illusion) is a popular optical illusion where it is impossible to state if a spinning dancer is rotating clockwise or anti-clockwise when given only the silhouette of the dancer and certain viewing geometries. In Figure 24, the middle column shows four frames of the rotating silhouette of a human figure, and both clockwise (left) and counter-clockwise (right) rotation of the human figure produces the same silhouette.\*

In the case of human figures, since we have a fair idea of the human shape model, we might be able to disambiguate between the two rotation vectors by changing the viewing geometry.<sup>19</sup> But in the case of unknown shape model, disambiguation between the two rotation vectors is significantly harder as merely changing the viewing geometry is not sufficient.

It is well known in the computer-science literature that SFS algorithm leads to ambiguity, i.e., the same silhouette pattern (with respect to time) can be formed by two different objects (different shapes) with different trajectories.<sup>14</sup> This illusory pole is the reflection of the true pole across the observing geometry. Here we provide a theatrical proof for this ambiguity, which is currently not available in the literature.

**Theorem 1:** When the spacecraft is approaching the small body along a given  $RA(\beta)$ - $Dec(\gamma)$ , for every particle at  $\mathbf{x}_i(t_0) = (x_i(t_0), y_i(t_0), z_i(t_0))$  rotating about the pole  $\hat{\mathbf{e}}$  with angular velocity  $\omega$ , these exists another particle at

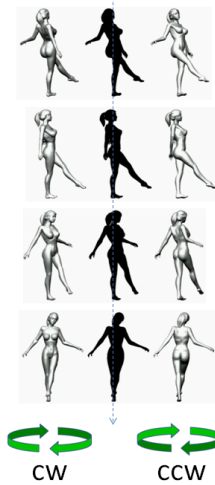


**Figure 24:** Image credit: Troje et. al.<sup>19</sup>

\*An animated version of this illustration can be found in [link](#).

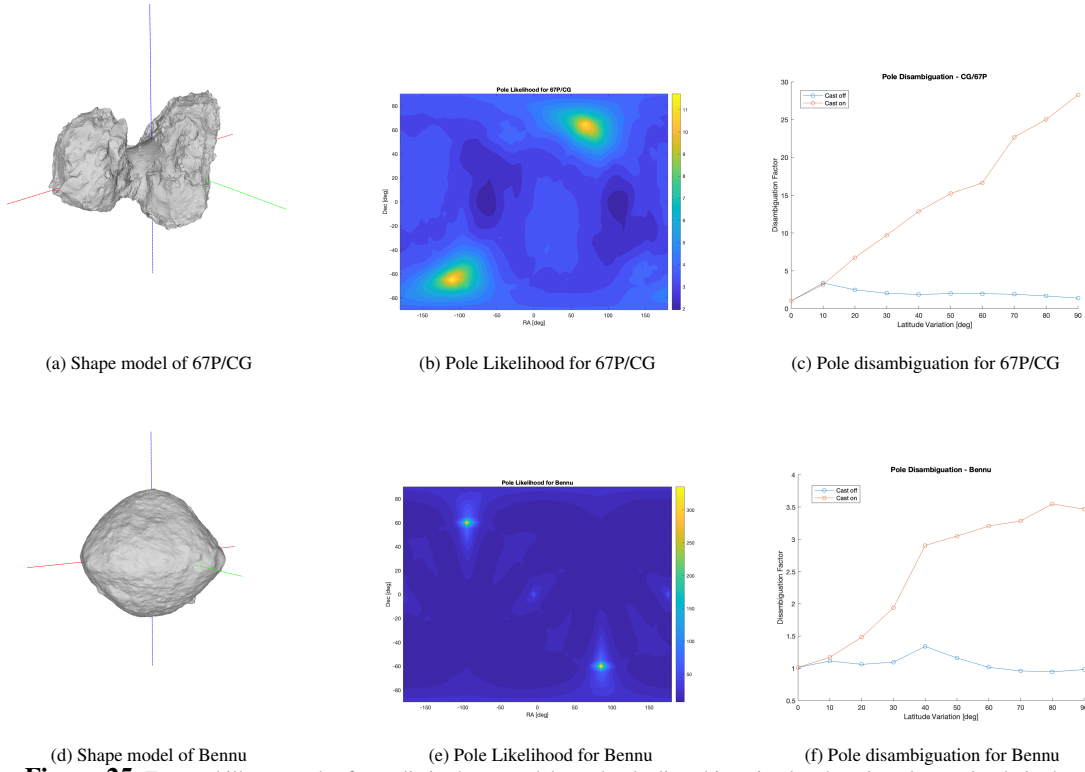


**Figure 25:** True and illusory poles for realistic shape models, and pole disambiguation by changing observation latitude

$\mathbf{x}_{i,new}(t_0)$  (Equation 10) rotating about the pole  $\hat{\mathbf{e}}_{new}$  (Equation 11) with angular velocity  $\omega$ , such that the trajectory tracked by the two particles in the image plane of the spacecraft’s camera is identical.

See proof in *Section Appendix: Proof of Theorem 1*.

For shape models of real small bodies like 67P/CG and Bennu, the true poles and the illusory poles for a spacecraft traveling in a straight line towards the small body are shown in Figure 25. Pole Likelihood distribution for 67P/CG in Figure 25b shows strong peaks near true pole (RA, Dec) = (65°, 65°) and illusory pole (RA, Dec) = (-110°, -65°). Pole Likelihood distribution for Bennu in Figure 25e shows strong peaks near true pole (RA, Dec) = (85°, -60°) and illusory pole (RA, Dec) = (-95°, 60°).

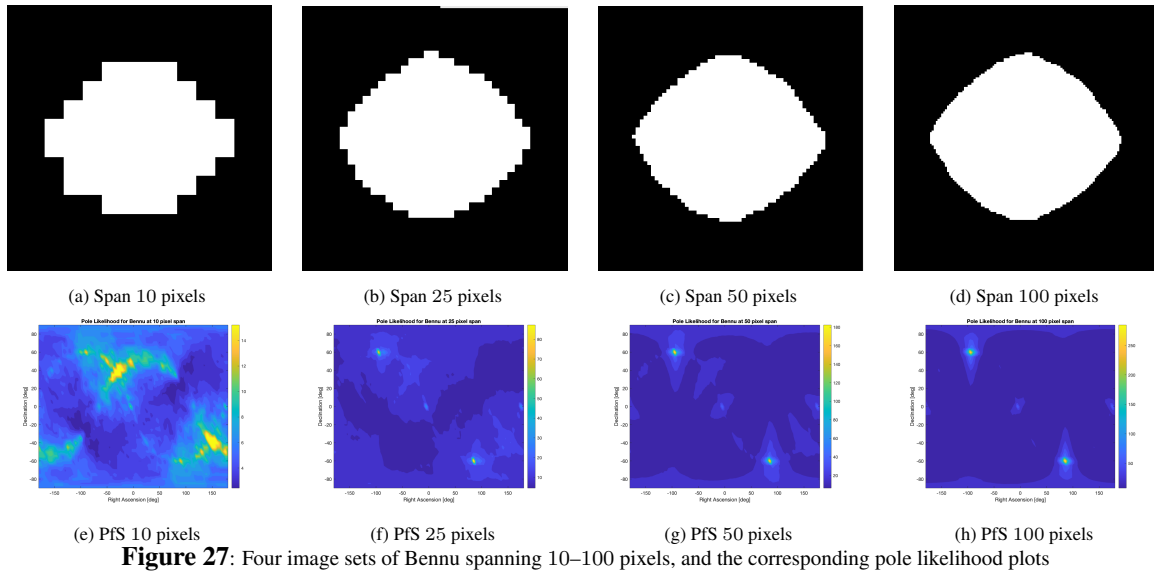
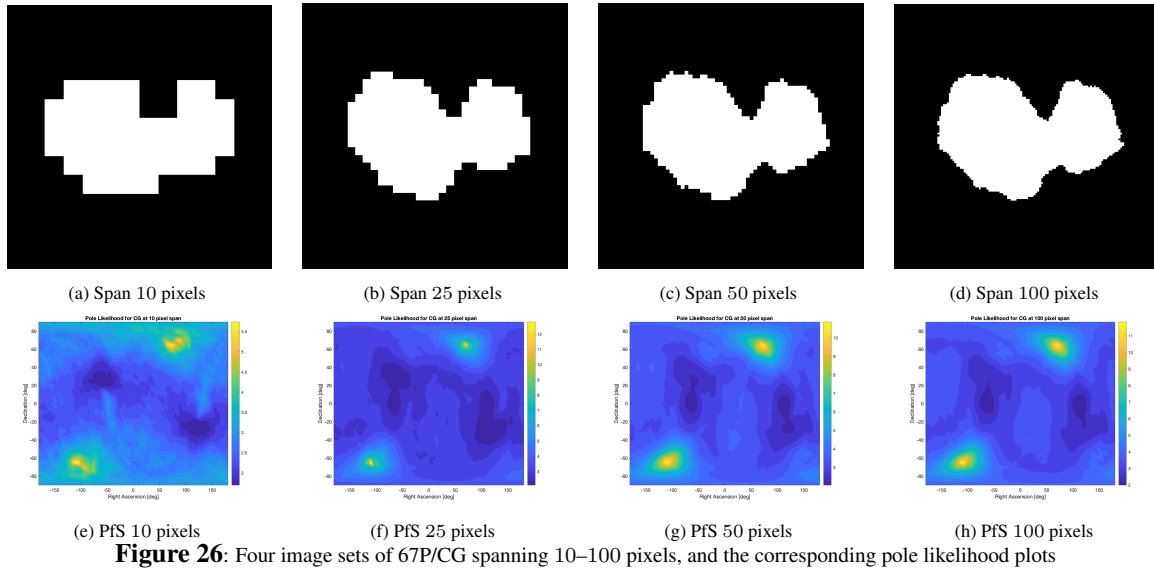
One approach to disambiguate between these poles is to change the observation latitude. Changing the observation latitude is only possible when the spacecraft is near the small body. Moreover such a maneuver usually introduces changes in the Sun phase angle, hence shadow-casting PSF algorithm (introduced in *Section Shadow Casting Algorithm for High Sun Phase Angles*) is preferred. Let us define the *disambiguation factor* as the ratio of likelihood score of true pole to that of illusory pole. The pole disambiguation by changing the observation latitude is shown in Figures 25c and 25f. Note that the asymmetry in the shape model of 67P/CG helps in the better disambiguation of the poles (as shown by the disambiguation factor in Figure 25c).

### Sensitivity to Image Size

A key advantage of the PfS algorithm is that it works even if the image size (i.e. span) of the small body is quite small. Figures 26 and 27 show the PfS solutions for the shape models of 67P/CG and Bennu, when their images span 10–100 pixels. The shape models of 67P/CG and Bennu used here, are shown in Figure 25.

As expected, a smaller image size (span) leads to lower pole likelihood scores for both shapes. For a highly asymmetric shape like 67P/CG, it is possible to estimate the pole even when the image size is as small as 10 pixels. On the other hand, for a close-to-symmetric body like Bennu, it is possible to estimate the pole

only when the image size is around 25 pixels. The effect of symmetry on the PfS algorithm’s performance is discussed in *Section Sensitivity to Different Shapes*.



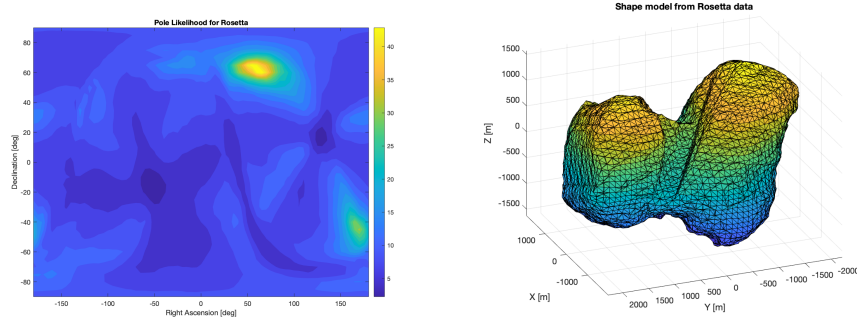
## APPLICATION TO REAL TRAJECTORY FROM THE ROSETTA MISSION

We autonomously execute the PfS and SfS algorithms with real data from the Rosetta mission. For PfS, we evaluate the Right Ascension (RA) range from  $-180^\circ$  to  $180^\circ$ , and Declination (Dec) range from  $-90^\circ$  to  $90^\circ$  with sample resolution of  $5^\circ$  on both axes. Figure 28a shows a clear peak due to the observation latitude variations in Rosetta’s trajectory. The SfS algorithm generates the visual hull of Rosetta at this peak pole estimate, as shown in Figure 28b.

The total computation run time to generate these results is approximately 3 hours, 44 minutes. This is significantly faster than the computation run time of the previous version of our SfS algorithm,<sup>11</sup> which took nearly a week for the same example and had unrealistic assumptions like perfect illumination.

## CONCLUSIONS

In this paper, we introduced the PfS and SfS algorithms that are important building blocks in the optical navigation pipeline for autonomous spacecraft approaching small bodies. We explained these algorithms in



(a) Pole Likelihood distribution using real data from Rosetta (b) SfS Shape Model using real Rosetta data  
**Figure 28:** PfS and SfS algorithm on real Rosetta data

detail and discussed the effects of different shapes, sun angles, viewing geometries on these algorithms. We are currently working on refining the visual hull by tracking visual features on the small body's surface and estimating their 3D positions. Future work will focus on making these algorithms more robust and tightly integrating them with the optical navigation pipeline so that they can also be used for ground operations for near-term mission to small bodies.

### ACKNOWLEDGMENTS

This research was carried out at the Jet Propulsion Laboratory, California Institute of Technology, under a contract with the National Aeronautics and Space Administration. ©2021 California Institute of Technology. Government sponsorship acknowledged.

### APPENDIX: PROOF OF THEOREM 1

We assume that the rays are parallel when they reach the camera, i.e, an orthographic or affine projection. Let the origin represent the center of rotation of the small body, and XYZ axis is in inertial frame. Let the pole of rotation of the small body be at RA= $\alpha$  and Dec= $\delta$ . The small body rotates with angular velocity  $\omega$  about its pole.

At time  $t_0$ , let the  $i^{\text{th}}$  particle on the small body be at  $(x_i(t_0), y_i(t_0), z_i(t_0))$ . At time  $t$ , this particle has rotated by angle  $\theta = \omega(t - t_0)$  about the pole. The Euler axis  $\hat{e}$  of the pole is given by:  $\hat{e} = \begin{pmatrix} \cos \delta \cos \alpha \\ \cos \delta \sin \alpha \\ \sin \delta \end{pmatrix}$ . The rotation matrix  $R(t)$  corresponding to an Euler axis  $\hat{e}$  and angle  $\theta = \omega(t - t_0)$  is given by  $R(t) = \mathbf{I} \cos \theta + (1 - \cos \theta) \hat{e} \hat{e}^T + [\hat{e}]_X \sin \theta$ , where

$$[\hat{e}]_X = \begin{pmatrix} 0 & -e_3 & e_2 \\ e_3 & 0 & -e_1 \\ -e_2 & e_1 & 0 \end{pmatrix} \text{ and } \mathbf{I} \text{ is identity matrix. The location of the } i^{\text{th}} \text{ particle at time } t \text{ is given by}$$

$$\begin{pmatrix} x_i(t) \\ y_i(t) \\ z_i(t) \end{pmatrix} = R(t) \begin{pmatrix} x_i(t_0) \\ y_i(t_0) \\ z_i(t_0) \end{pmatrix};$$

$$x_i(t) = ((1 - \cos \theta) \cos^2 \delta \cos^2 \alpha + \cos \theta) x_i(t_0) + ((1 - \cos \theta) \cos^2 \delta \cos \alpha \sin \alpha - \sin \delta \sin \theta) y_i(t_0) + ((1 - \cos \theta) \cos \delta \cos \alpha \sin \delta + \cos \delta \sin \alpha \sin \theta) z_i(t_0) \quad (3)$$

$$y_i(t) = ((1 - \cos \theta) \cos^2 \delta \sin \alpha \cos \alpha + \sin \delta \sin \theta) x_i(t_0) + ((1 - \cos \theta) \cos^2 \delta \sin^2 \alpha + \cos \theta) y_i(t_0) + ((1 - \cos \theta) \cos \delta \sin \alpha \sin \delta - \cos \delta \cos \alpha \sin \theta) z_i(t_0) \quad (4)$$

$$z_i(t) = ((1 - \cos \theta) \sin \delta \cos \delta \cos \alpha - \cos \delta \sin \alpha \sin \theta) x_i(t_0) + ((1 - \cos \theta) \sin^2 \delta + \cos \theta) z_i(t_0) + ((1 - \cos \theta) \sin \delta \cos \delta \sin \alpha + \cos \delta \cos \alpha \sin \theta) y_i(t_0) \quad (5)$$

**Special Case: Approach along X-axis:** If the spacecraft approaches the small body along the X-axis, then the spacecraft observes the trajectory of the  $i^{\text{th}}$  particle projected on the Y-Z plane given by Eq. (4) and

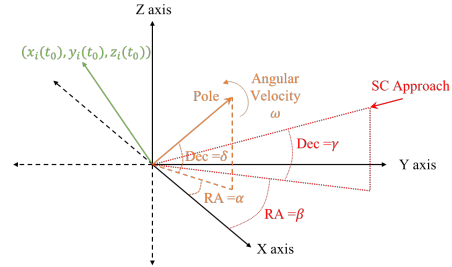


**Figure 29:** Reference Frame showing Small Body's center of mass as the origin, and approaching SC

(5). It is easy to see that a particle at  $(-x_i(t_0), y_i(t_0), z_i(t_0))$  rotating about the pole at RA= $-\alpha$  and Dec= $-\delta$  with angular velocity  $\omega$  will project the same trajectory in the Y-Z plane:

$$\begin{aligned} \hat{y}_i(t) &= ((1 - \cos \theta) \cos^2 \delta \sin \alpha \cos \alpha + \sin \delta \sin \theta) x_i(t_0) + ((1 - \cos \theta) \cos^2 \delta \sin^2 \alpha + \cos \theta) y_i(t_0) \\ &\quad + ((1 - \cos \theta) \cos \delta \sin \alpha \sin \delta - \cos \delta \cos \alpha \sin \theta) z_i(t_0) = y_i(t) \text{ in Eq. (4)} \end{aligned} \quad (6)$$

$$\begin{aligned} \hat{z}_i(t) &= ((1 - \cos \theta) \sin \delta \cos \delta \cos \alpha - \cos \delta \sin \alpha \sin \theta) x_i(t_0) + ((1 - \cos \theta) \sin^2 \delta + \cos \theta) z_i(t_0) \\ &\quad + ((1 - \cos \theta) \sin \delta \cos \delta \sin \alpha + \cos \delta \cos \alpha \sin \theta) y_i(t_0) = z_i(t) \text{ in Eq. (5)} \end{aligned} \quad (7)$$

Therefore, it is impossible to disambiguate between (i) the particle at  $\mathbf{x}_i(t_0) = (x_i(t_0), y_i(t_0), z_i(t_0))$  rotating about the pole at RA= $\alpha$  and Dec= $\delta$  with angular velocity  $\omega$ , and (ii) a new particle at  $\mathbf{x}_{i,new}(t_0) = (-x_i(t_0), y_i(t_0), z_i(t_0))$  rotating about the pole at RA= $-\alpha$  and Dec= $-\delta$  with angular velocity  $\omega$ . Note that we get the following transformations for this new particle initial position  $\mathbf{x}_{i,new}(t_0)$  and new pole  $\hat{\mathbf{e}}_{new}$ :

$$\mathbf{x}_{i,new}(t_0) = \begin{pmatrix} -1 & 0 & 0 \\ 0 & 1 & 0 \\ 0 & 0 & 1 \end{pmatrix} \mathbf{x}_i(t_0), \quad \hat{\mathbf{e}}_{new} = \begin{pmatrix} 1 & 0 & 0 \\ 0 & -1 & 0 \\ 0 & 0 & -1 \end{pmatrix} \hat{\mathbf{e}} \quad (8)$$

Hence the SfS algorithm will generate two shapes with two different pole locations. Due to the one-to-one mapping between the particles, it is obvious that the two shapes are mirror images of each other (reflected about Y-Z plane).

**General Case: Approach along any direction:** Let the spacecraft approach the small body along RA= $\beta$  and Dec= $\gamma$ . The spacecraft approach vector is given by  $\begin{pmatrix} \cos \gamma \cos \beta \\ \cos \gamma \sin \beta \\ \sin \gamma \end{pmatrix}$ . The rotation matrix to convert the spacecraft approach vector to  $\begin{pmatrix} 1 \\ 0 \\ 0 \end{pmatrix}$  is denoted by  $R_{SC}$ :

$$\begin{pmatrix} 1 \\ 0 \\ 0 \end{pmatrix} = R_{SC} \begin{pmatrix} \cos \gamma \cos \beta \\ \cos \gamma \sin \beta \\ \sin \gamma \end{pmatrix}, \quad \text{where } R_{SC} = \begin{pmatrix} \cos \gamma \cos \beta & \cos \gamma \sin \beta & \sin \gamma \\ -\sin \beta & \cos \beta & 0 \\ -\cos \beta \sin \gamma & -\sin \beta \sin \gamma & \cos \gamma \end{pmatrix} \quad (9)$$

Our proof technique is to rotate the reference frame such that the spacecraft is approaching along the new X-axis. Then we can use the result from the previous special case. The Euler axis of the pole in the rotated reference frame is given by  $\hat{\mathbf{e}}_{rot} = R_{SC} \begin{pmatrix} \cos \delta \cos \alpha \\ \cos \delta \sin \alpha \\ \sin \delta \end{pmatrix}$ . Similarly, the  $i^{\text{th}}$  particle in the rotated reference frame is given by  $\mathbf{x}_{i,rot}(t_0) = R_{SC} \begin{pmatrix} x_i(t_0) \\ y_i(t_0) \\ z_i(t_0) \end{pmatrix}$ . The new particle's position and new pole, which cannot be disambiguated in the rotated reference frame, follows from the transformation in the previous case (Equation 8). The new particle position and pole Euler axis in the inertial reference frame are:

$$\mathbf{x}_{i,new}(t_0) = R_{SC}^T \mathbf{x}_{i,rot,new}(t_0) = R_{SC}^T \begin{pmatrix} -1 & 0 & 0 \\ 0 & 1 & 0 \\ 0 & 0 & 1 \end{pmatrix} R_{SC} \begin{pmatrix} x_i(t_0) \\ y_i(t_0) \\ z_i(t_0) \end{pmatrix} \quad (10)$$

$$\hat{\mathbf{e}}_{new} = R_{SC}^T \hat{\mathbf{e}}_{rot,new} = R_{SC}^T \begin{pmatrix} 1 & 0 & 0 \\ 0 & -1 & 0 \\ 0 & 0 & -1 \end{pmatrix} R_{SC} \begin{pmatrix} \cos \delta \cos \alpha \\ \cos \delta \sin \alpha \\ \sin \delta \end{pmatrix} \quad (11)$$

Therefore, when the spacecraft is approaching the small body along RA= $\beta$  and Dec= $\gamma$ , it is impossible to disambiguate between (i) a particle at  $(x_i(t_0), y_i(t_0), z_i(t_0))$  rotating about the pole  $\hat{\mathbf{e}}$  with angular velocity  $\omega$ , and (ii) a particle at  $\mathbf{x}_{i,new}(t_0)$  (Equation 10) rotating about the pole  $\hat{\mathbf{e}}_{new}$  (Equation 11) with angular velocity  $\omega$  where  $R_{SC}$  is defined in Equation 9.

## REFERENCES

- [1] D. DellaGiustina, J. Emery, D. Golish, B. Rozitis, C. Bennett, K. Burke, R.-L. Ballouz, K. Becker, P. Christensen, C. D. d'Aubigny, *et al.*, "Properties of rubble-pile asteroid (101955) Benu from OSIRIS-REx imaging and thermal analysis," *Nature Astronomy*, Vol. 3, No. 4, 2019, pp. 341–351.
- [2] K. Kitazato, R. Milliken, T. Iwata, M. Abe, M. Ohtake, S. Matsuura, T. Arai, Y. Nakauchi, T. Nakamura, M. Matsuoka, *et al.*, "The surface composition of asteroid 162173 Ryugu from Hayabusa2 near-infrared spectroscopy," *Science*, Vol. 364, No. 6437, 2019, pp. 272–275.
- [3] D. Yeomans, P. Antreasian, J.-P. Barriot, S. Chesley, D. Dunham, R. Farquhar, J. Giorgini, C. Helfrich, A. Konopliv, J. McAdams, *et al.*, "Radio science results during the NEAR-Shoemaker spacecraft rendezvous with Eros," *Science*, Vol. 289, No. 5487, 2000, pp. 2085–2088.

- [4] F. Capaccioni, A. Coradini, G. Filacchione, S. Erard, G. Arnold, P. Drossart, M. De Sanctis, D. Bockelee-Morvan, M. Capria, F. Tosi, *et al.*, “The organic-rich surface of comet 67P/Churyumov-Gerasimenko as seen by VIRTIS/Rosetta,” *Science*, Vol. 347, No. 6220, 2015, p. aaa0628.
- [5] D. Scheeres, J. McMahon, J. Wood, E. Bierhaus, L. Benner, C. Hartzell, P. Hayne, J. Hopkins, R. Jedicke, L. LeCorre, *et al.*, “Janus: A NASA SIMPLEX mission to explore two NEO Binary Asteroids,” *Euromet Science Congress*, Vol. 14, 1965.
- [6] E. Adams, D. O’Shaughnessy, M. Reinhard, J. John, E. Congdon, D. Gallagher, E. Abel, J. Atchison, Z. Fletcher, M. Chen, *et al.*, “Double Asteroid Redirection Test: The Earth Strikes Back,” *2019 IEEE Aerospace Conference*, IEEE, 2019, pp. 1–11.
- [7] S. Papais, B. J. Hockman, S. Bandyopadhyay, R. R. Karimi, S. Bhaskaran, and I. A. Nefnas, “Architecture Trades for Accessing Small Bodies with an Autonomous Small Spacecraft,” *2020 IEEE Aerospace Conference*, Big Sky, MT, IEEE, March 2020.
- [8] T. D. Swindle, I. A. Nefnas, and J. C. Castillo-Rogez, “Design Reference Missions (DRMs) for Advancing Autonomy in Exploration of Small Bodies,” *AGUFM*, Vol. 2019, 2019, pp. IN34A–08.
- [9] J. Villa, S. Bandyopadhyay, B. Morrell, B. J. Hockman, D. Lubey, A. Harvard, S.-J. Chung, S. Bhaskaran, and I. A. Nefnas, “Optical Navigation for Autonomous Approach of Unexplored Small Bodies,” *AAS Guidance, Navigation and Control Conference*, Breckenridge, Colorado, IEEE, Feb. 2020.
- [10] I. Nefnas, B. Hockman, S. Bandyopadhyay, B. Morrell, D. Lubey, J. Villa, D. Bayard, A. Osmundson, B. Jarvis, M. Bersani, and S. Bhaskaran, “Autonomous Exploration of Small Bodies Toward Greater Autonomy for Deep Space Missions,” *Frontiers in Robotics and AI*, 2021. submitted.
- [11] S. Bandyopadhyay, I. Nefnas, S. Bhaskaran, B. Hockman, and B. Morrell, “Silhouette-Based 3D Shape Reconstruction of a Small Body from a Spacecraft,” *2019 IEEE Aerospace Conference*, IEEE, 2019, pp. 1–13.
- [12] W. N. Martin and J. K. Aggarwal, “Volumetric descriptions of objects from multiple views,” *IEEE transactions on pattern analysis and machine intelligence*, No. 2, 1983, pp. 150–158.
- [13] K. Cheung, S. Baker, and T. Kanade, “Shape-from-silhouette of articulated objects and its use for human body kinematics estimation and motion capture,” *2003 IEEE Computer Society Conference on Computer Vision and Pattern Recognition, 2003. Proceedings.*, Vol. 1, IEEE, 2003, pp. 1–1.
- [14] S. Baker, T. Kanade, *et al.*, “Shape-from-silhouette across time part I: Theory and algorithms,” *International Journal of Computer Vision*, Vol. 62, No. 3, 2005, pp. 221–247.
- [15] S. Savarese, M. Andreetto, H. Rushmeier, F. Bernardini, and P. Perona, “3D reconstruction by shadow carving: Theory and practical evaluation,” *International journal of computer vision*, Vol. 71, No. 3, 2007, pp. 305–336.
- [16] A. Laurentini, “The visual hull concept for silhouette-based image understanding,” *IEEE Transactions on pattern analysis and machine intelligence*, Vol. 16, No. 2, 1994, pp. 150–162.
- [17] M. Lauer, S. Kielbassa, and R. Pardo, “Optical measurements for attitude control and shape reconstruction at the Rosetta flyby of asteroid Lutetia,” *ISSFD2012 paper, International Symposium of Space Flight Dynamics, Pasadena, California, USA*, 2012.
- [18] R. P. d. Santayana and M. Lauer, “Optical measurements for rosetta navigation near the comet,” *Proceedings of the 25th International Symposium on Space Flight Dynamics (ISSFD), Munich*, 2015.
- [19] N. F. Troje and M. McAdam, “The viewing-from-above bias and the silhouette illusion,” *i-Perception*, Vol. 1, No. 3, 2010, pp. 143–148.
- [20] S. Bhaskaran, “Autonomous navigation for deep space missions,” *SpaceOps 2012*, pp. 126–135, American Institute of Aeronautics and Astronautics, 2012.
- [21] K. Forbes, *Calibration, recognition, and shape from silhouettes of stones*. PhD thesis, University of Cape Town, 2007.
- [22] W. M. Owen Jr, “Methods of optical navigation,” 2011.
- [23] P. G. Antreasian, M. C. Moreau, C. D. Adam, A. French, J. Geeraert, K. M. Getzandanner, D. E. Highsmith, J. M. Leonard, E. J. Lessac-Chenen, A. H. Levine, *et al.*, “Early navigation performance of the OSIRIS-REx approach to Bennu,” 2019.